https://doi.org/10.1016/j.jmapro.2019.02.005

Microstructural effects of Ti6Al4V alloys modified by electropulsing treatment on ultraprecision diamond turning

Zejia Zhao[a], Suet To[a,*], Zhanwen, Sun[a], Renjie, Ji[b] and Kai Ming Yu[a]

[a]State Key Laboratory of Ultra-precision Machining Technology, Department of Industrial and Systems Engineering, The Hong Kong Polytechnic University, Hung Hom, Kowloon, Hong Kong SAR, China

[b]College of Mechanical and Electronic Engineering, China University of Petroleum (East China), Qingdao, Shandong, 266580, PR China

* Corresponding author. Tel.: +852 2766 6587.
E-mail address: sandy.to@polyu.edu.hk (S. To).

Abstract

The mechanical properties of polycrystalline materials are significantly affected by their microstructures, such as the grain size, phase composition and texture. In this paper, Ti6Al4V alloys with equiaxed grain structure, bimodal structure and martensitic structure are obtained by electropulsing treatment (EPT). The microstructural evolution is primarily caused by the coupling function of thermal and athermal effects of EPT. A theoretical model was built to analyze the temperature evolution induced by the thermal effect of EPT from the perspectives of energy gain, heat transfer and thermal radiation. Ultraprecision diamond turning was then conducted to investigate the effects of microstructures on the machinability of Ti6Al4V alloys. The results show that material swelling and spring-back vary with microstructures due to the various strength and ductility, which significantly affects the turning surface profiles. The alloy with fully martensitic structure shows a best surface roughness of approximately 9 nm after diamond turning, and the cutting and thrust forces are also lower than the alloys with equiaxed and bimodal structures. The paper also qualitatively analyzes the cutting and thrust force evolution of the alloys with various microstructures.

Keywords: Ti6Al4V alloys; Electropulsing treatment (EPT); Microstructures; Ultraprecision diamond turning; Cutting and thrust forces.

1. Introduction

High-strength and light weight metal materials, such as magnesium (Mg) alloys, beryllium (Be) alloys and titanium (Ti) alloys, have been widely developed to meet the rising demands for manufacturing of key components used in high performance applications [1-3]. Among them, titanium alloys have been attracting a great deal of attention for several decades due to their superior biocompatibility and excellent mechanical properties, including high strength, great corrosion resistance and exceptional fracture toughness, especially for the two phase Ti6Al4V alloy. The mechanical properties of the Ti6Al4V alloy are directly affected by its microstructures which can be altered through proper heat treatment followed by different cooling rates. Fully slender martensitic α lamellas could be achieved after annealing in single β phase followed by high cooling rates (above 410 °C/s) or water quenching, while thick lamellar structures would be obtained if the cooling at low rates in furnace [4, 5]. With a moderate cooling rate, in the air for example, the microstructure is composed of primary α phase and some acicular phase in the β matrix [6]. The yield strength, cycle fatigue and fracture toughness of titanium alloy with fully slender α lamellas are superior to those with coarse lamellar structure. The bimodal structure consisting of primary α phase and α/β lamellas usually gives rise to high ductile features compared with the fully lamellar structure and equiaxial crystal structure possessing moderate strength and ductility [7].

In comparison to the traditional furnace annealing process, the electropulsing treatment (EPT) is a more efficient and time saving technique in altering material microstructures and facilitating phase transformation. In 1970s, Troitskii et al. [8] proposed that the reduction of flow stress and the increase of elongation of metals are due to the dislocation movement under electron wind condition. Actually, electrical pulses have two kinds of effects on changing microstructure of metal materials: thermal effect and athermal effect. Zhang et al. [9] investigated the effect of thermal energy induced by electropulsing on the microstructure evolution of four kinds of materials, and the authors also theoretically calculated the instantaneous temperature change and discussed that the possible mechanisms for nano-structure transition may be attributed to the rapid heating and cooling rates, thermal stress and thermodynamic energy barrier. To et al. [10, 11] studied the athermal effects of electropulsing on phase transformations of Zn-Al alloy from the views of Gibbs free energy and electropulsing kinetics. The authors found that phase transformations can be effectively accelerated by the current density, which is mainly due to electron wind force that influences the fluxes of dislocations and vacancies. In the study conducted by Tang et al. [12], the coupling thermal and athermal effects of EPT for several seconds contribute to an accelerating dissolution rate for β phase in an aged Mg–9Al–1Zn alloy, which is considered to be induced by the decreasing phase nucleation thermodynamic barrier and the improvement of atomic diffusion. The microstructure evolution of the Ti6Al4V alloy after EPT was also investigated in recent years, and the strength and ductility of this material were found to vary with EPT parameters [13-15].

The Ti6Al4V alloy is known as one of difficult-to-cut materials due to the poor thermal conductivity, low modulus of elasticity and serious chemical reaction [16, 17]. A wide variety of studies have been conducted to address the machining problems of Ti6Al4V alloys by adopting suitable liquid cooling systems aiming at facilitating heat dissipation at cutting zones [18-20], but those researches were conducted from the perspective of improving external conditions instead of altering the alloy intrinsic nature. As the inherent properties of metals and alloys are greatly affected by the microstructures, the machinability of the Ti6Al4V alloy in ultraprecision diamond turning should be closely correlated to its microstructures, such as phase composition, phase and grain sizes. Nouari and Makich [21] found that the tool wear could be affected by microstructure evolution during machining Ti6Al4V and Ti-555 alloys. Armendia et al [22] also studied the tool wear and cutting forces of Ti6Al4V alloy with various microstructures in traditional turning processes. Besides, the effects of microstructures on cutting force and built-up edge (BUE) have also been investigated during milling of Ti6Al4V alloys [23, 24]. Though some studies have been conducted on investigating the influences of various microstructures on the cutting force, tool wear and BUE of Ti6Al4V alloys in conventional machining, little research has been carried out on investigating the machinability of the Ti6Al4V alloy with different microstructures from the perspectives of material spring-back and swelling in ultraprecision diamond turning. Therefore, the purpose of this study is to explore the machinability of Ti6Al4V alloys with three typical microstructures produced by high efficient of EPT. In addition, the temperature evolution caused by the thermal effect of EPT is theoretically and experimentally analyzed, and the cutting force variation in ultraprecision machining is discussed.

2. Experimental procedures

The Ti6Al4V (Ti-5.900Al-4.032V-0.075Fe-0.018C-0.030N-0.12O-0.001H) alloy with a diameter of 3 mm was used for EPT and ultraprecision machining. The EPT was conducted on a commercial electropulsing device (THDM-III) that has been stated in our previous study [25]. A sketch of EPT sample fixture setup with real-time temperature measurement method is shown in Fig. 1. Voltages, frequencies and corresponding effective current densities of EPT are tabulated in Table 1. After EPT for 2 minutes, all samples were immediately cooled in the water. Then, the alloys were mechanically cut into samples with a dimension of Φ3 mm × 6 mm for the following metallographic observation, compressive test and ultraprecision machining. The essential steps of metallographic sample preparation include thermal mounting, mechanical grinding, electrical polishing in a mixed solution of $HClO_4$: CH_3COOH (1:16) and chemical etching (HF: HNO_3: H_2O=1:3:5).

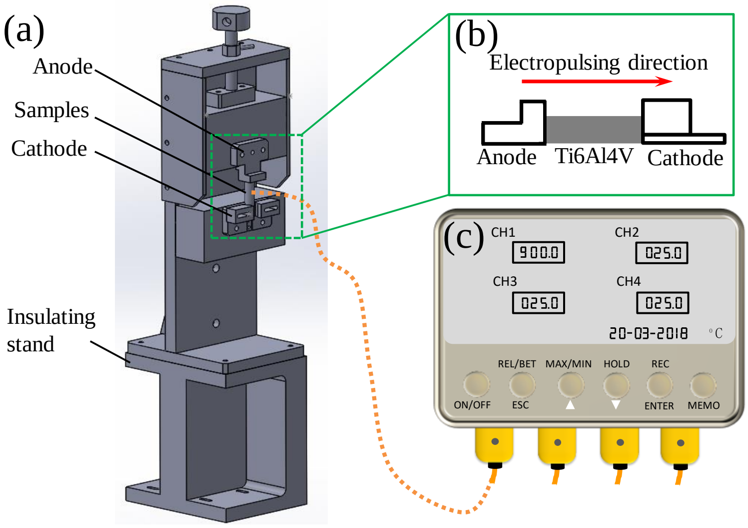

Fig. 1 Schematics of (a) sample fixture of EPT, (b) sample treatment during EPT and (c) real-time temperature measurement by a digital thermocouple with record function

Table 1 EPT parameters and corresponding measured peak temperature

Sample No.	Voltage (V)	Frequency (Hz)	J_e (A/m^2)	Peak temperature (°C)
1	-	-	-	-
2	30	300	5.60×10^7	529
3	40	300	7.92×10^7	802
4	60	300	1.24×10^8	1270

The ultraprecision diamond turning was conducted on a 4-axis ultra-precision machine Moore Nanotech 350FG. A fresh diamond tool with a nose radius of 1.0002 mm, rake angle of 0° and front clearance angle of 12.5° was utilized for turning. Rough machining was carried out firstly to flatten the surface, and then finish diamond turning was executed at a spindle speed of 1000 rpm, cutting depth of 3 μm and feed rate of 4 mm/min. A force sensor (Kistler 9256C1) was mounted under the fresh cutting tool to measure the cutting and thrust forces. All the turning experiments were repeated three times. The phase transformation was estimated by a differential scanning calorimetry (DSC, STA 449 F3 Jupiter thermal analyzer) with temperature ranging from 25 °C to 1200 °C at a heating rate of 5 °C/min under an air atmosphere. The phase composition was identified by a high resolution X-ray diffractometer (HRXRD) with a scanning rate of 3 °/min. The electronic morphologies were obtained by a scanning electron microscope (SEM, Tescan VEGA3). A Nexview three-dimension (3D) optical surface profiler (Zygo) and an atomic force microscope (AFM, Park's XE-70) were used to obtain the surface topographies and tool mark profiles. The Vickers hardness was measured by a Mitutoyo testing machine under a load of 0.2 kg, and the Young's moduli were measured by a Nano Indenter G200. The oxygen contents of the alloys were detected by the LECO combustion analyzer ONH836.

3. Results and discussion

3.1 Material characteristics

Fig. 2 shows the differential scanning calorimetry (DSC) curve of the virgin Ti6Al4V alloy. Three endothermic peaks representing phase transformation from α to β phase are obviously observed in the curve, corresponding to temperatures of about 705°C, 920°C and 1085°C, respectively. The first low temperature peak stands for the onset of decomposition of α phase, and the high temperature (above 920 °C) peaks represent the phase transformation of primary α phase to β phase [26]. Hence, α phase starts to transform to β phase at temperature around 705°C, and the transformation prevails at above 920 °C. The endothermic peak at temperature of about 1085°C is supposedly due to the rapid grains growth of the β phase [27].

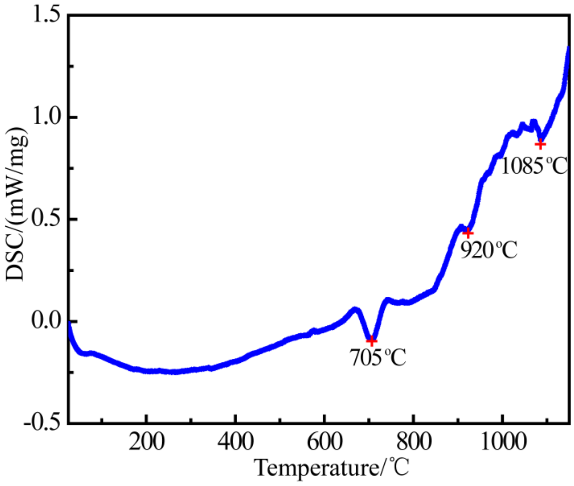

Fig. 2 DSC curve of the virgin Ti6Al4V alloy

Fig. 3 shows the electronic morphologies of Ti6Al4V samples under different EPT parameters. The virgin Ti6Al4V alloy is composed of α phase within β matrix. The average β particles after 30 V, 300 Hz followed by water quench increase from about 0.5 μm to 1.5μm, and the volume fraction of β phase also shows an increment in comparison to the virgin Ti6Al4V alloy, as illustrated in Fig. 3 (b). As the specimen temperature after EPT of 40 V and 300 Hz can reach as high as 802 °C that is higher than the first phase transformation temperature of 705 °C, a large amount of short secondary α lamellas are observed to nucleate within β grains after water quench, forming α/β lamellas. This results in the final microstructure mainly consisting of primary equiaxed α grains and α/β lamellas, as shown in Fig. 3 (c). For EPT of 60V and 300 Hz, substantial lamellar α martensite is formed in β grains after quenching, but the length of the majority of α lamellas is quite longer than that of 40 V and 300 Hz. In addition, the distribution of α lamellas shows orthotropic feature, which results from the lamellar nucleation process from single β phase. The α is constituted of long martensitic platelets with an acicular morphology [4], and the growth of α would not stop until they met other α platelets of different variant of the Burgers orientation relationship (BOR) in the same β grain [28].

The X-ray diffraction (XRD) patterns of Ti6Al4V alloy with different microstructures are given in Fig. 4. At electropulsing voltages of 0 V and 30 V, β phase with body centered cubic crystal structure can be detected by the XRD, but with further increasing of voltages, the peak of β phase eventually disappears, which indicates that the volume fraction of β phase reduces at voltages above 40 V. According to the SEM morphologies given in Fig. 3 (a) and (b), and by using ASTM E1245 criteria, the volume fraction of β phase is calculated to be 10 ± 3 % and 20 ± 3 % of the total volume for virgin and EPT (30 V, 300 Hz) treated samples, respectively. The low volume fraction contributes to the weak XRD peak of the β phase. Even β grains shown in Fig. 3 (c) are not fully occupied by the secondary α lamellas after water quench, the β phase cannot be identified by the XRD due to the quite low content. For water quench from about 1270 °C (EPT of 60V, 300 Hz), the prevalence microstructure is detected to be α martensites. Jovanović et al. [6] pointed out that the volume fraction of β phase accounts for merely 1.3 % of the total volume for quenching Ti6Al4V alloy from high temperatures.

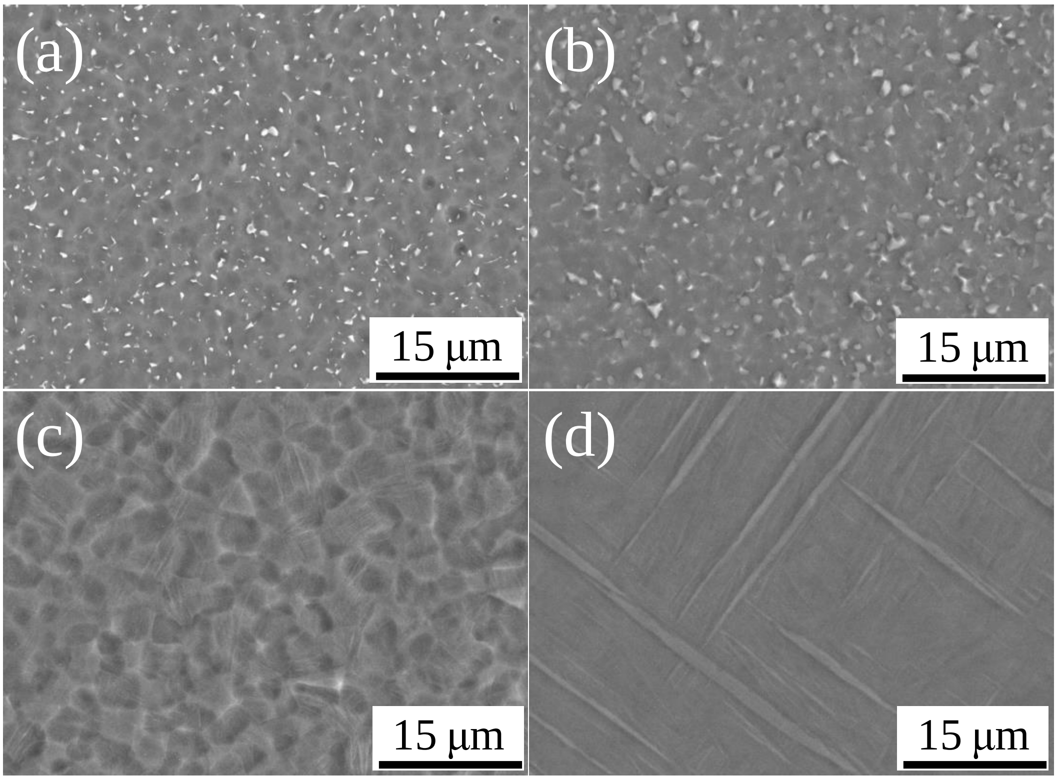

Fig. 3 SEM morphologies of (a) virgin and EPT treated samples after (b) 30 V, 300 Hz, (c) 40 V, 300 Hz and (d) 60 V, 300 Hz

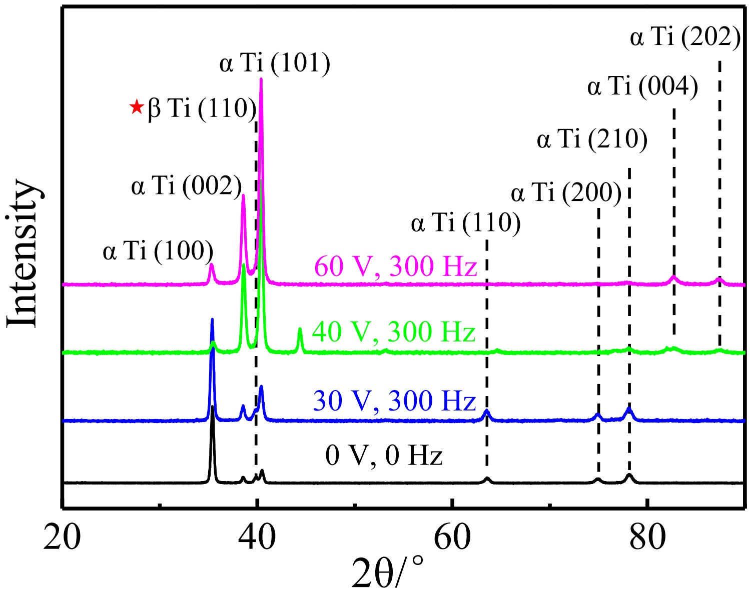

Fig. 4 XRD patterns of Ti6Al4V alloys under different EPT conditions

The Vickers microhardness variation of Ti6Al4V alloys with four types of microstructures is illustrated in Fig. 5. The average microhardness of the virgin alloy is about 315 HV, and it slightly decreases to about 290 HV after EPT of 30 V and 300 Hz. As electropulsing voltage further increases to 40 V, the average microhardness reversely increases by 40 HV compared with the virgin samples. Interestingly, the hardness curve of Ti alloys after 60 V, 300 Hz shows a symmetrical character along the diameter. The mean value of hardness within a diameter of about 1 mm is comparable with that of after EPT of 40 V, but it rapidly increases with elongation of diameter, reaching a highest value of about 460 HV at the outermost of the cylinder workpiece.

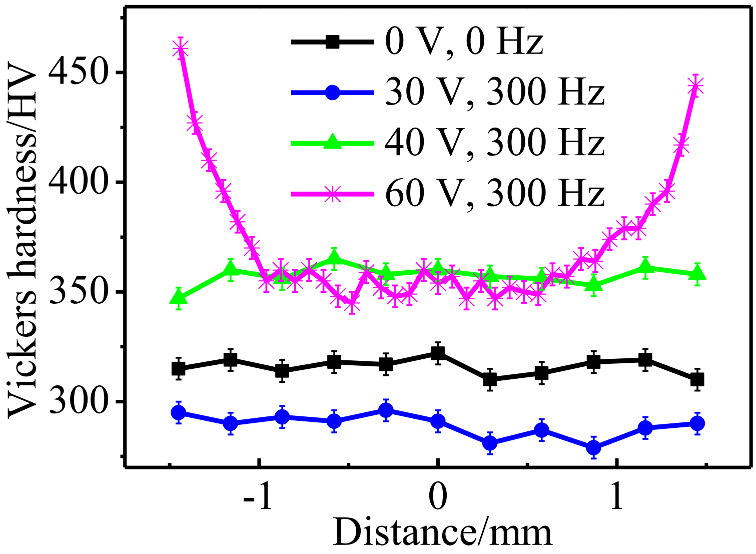

Fig. 5 Vickers microhardness variation of Ti6Al4V alloys

The gradient distribution of hardness of alloy after EPT of 60 V and 300 Hz mainly results from the different oxygen contents and cooling rates between the outside and center of the sample. As the alloy treatments were conducted in unprotected atmosphere, oxygen contamination of surface layer could occur during EPT process. The oxygen contents of the outside workpiece with a thickness of about 0.2 mm and the centre bulk region with a diameter of about 1.3 mm are about 0.180 ± 0.01 wt % and 0.125 ± 0.01 wt %, respectively. Hence, the high oxygen content in the outside region of titanium alloy could induce a high hardness, which has also been proposed by Bermingham et al. [29] in additive manufacturing of Ti6Al4V alloys. Besides, the size and thickness of the martensite could become larger with reduction of cooling rates according to references [30, 31], the size and thickness of the martensite could become larger with reduction of cooling rates. A similar result was also found in the EPT treated alloys, as shown in Fig. 6 (a) and (b). In outside of EPT treated alloy, the martensitic thickness is much smaller than that of the inside martensite, and the density of martensite is higher than the inside ones due to a relative large cooling rate. As the small thickness and large density of martensite give rise to more phase boundaries, the deformation resistance of the outside should be larger than the inside, contributing to the symmetrical hardness distribution along the diameter.

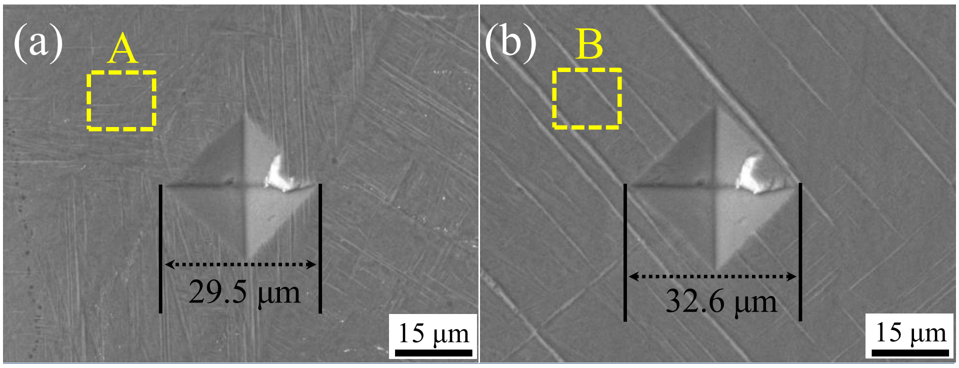

Fig. 6 SEM Morphologies of Vickers hardness indentation imprints and martensitic microstructures of Ti6Al4V alloy at radius of (a) 1.36 mm and (b) 0.72 mm

3.2 Cutting surface morphologies

Fig. 7 presents the SEM and 3D Zygo morphologies of different Ti6Al4V alloys after ultraprecision diamond turning under the same cutting condition. As illustrated in Fig. 7 (a) and (c), the turning profiles of samples without treatment and treated by EPT of 40 V show no obvious distinction, both having irregular distribution of tool marks. It is worth noting that many bulges (black arrows) are observed in the EPT treated alloys, while few are found in the virgin alloy. This phenomenon can also be verified by the 3D morphologies given in Fig. 7 (g) where abundant intermittent bulges are distributed uniformly in the turning surface, so the area surface roughness S_a of the EPT treated alloy (23 nm) is slightly higher than that of without treatment

(20 nm). For EPT of 30 V and 60 V, homogeneous diamond turning tool marks can be achieved on the surface after ultraprecision machining. However, the S_a of the latter sample can reach about 9 nm, which is much smaller than the former with S_a of 52 nm, as presented in Fig. 7 (f) and (h).

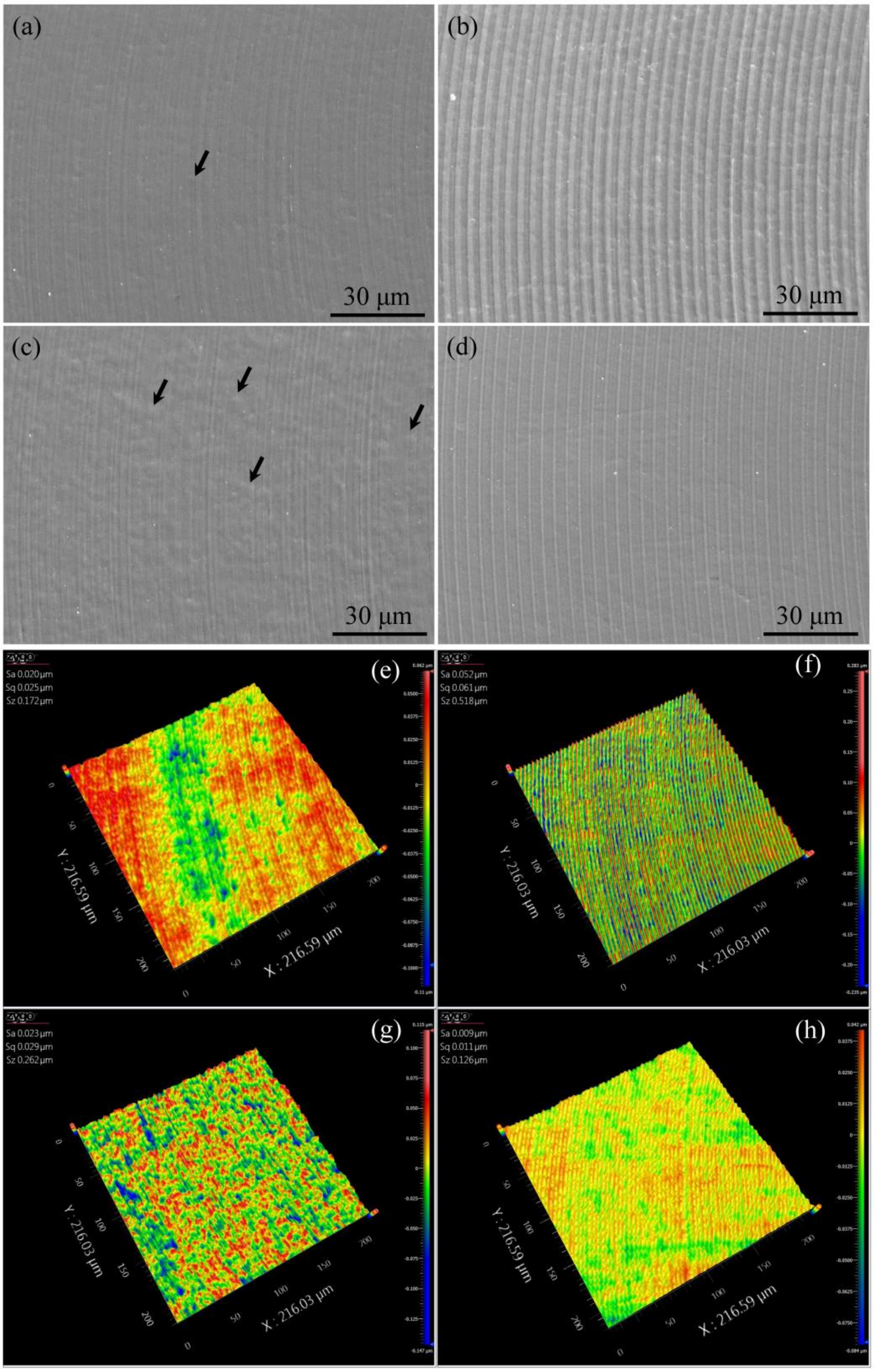

Fig. 7 Tool marks of SEM morphologies for samples of (a) without EPT and EPT of

(a) 30 V, (b) 40 V and (d) 60 V; (e)-(g) are corresponding 3-D topographies.

The cross-section profiles of turning surfaces measured by Zygo are shown in Fig. 8. It can be seen that the peak to valley (PV) values of all specimen are much higher than the theoretical values ($R_t = \frac{f^2}{8RV^2}$), which is attributed to the combined effect of material swelling and spring-back. Material side swelling could introduce slightly wider turning marks than the ideal width, while deep swelling could lead to much deeper marks than the ideal mark height and it is more significant than the side swelling [32]. The coupling effects of side and deep swelling could result in a large surface roughness. On the contrary, the spring-back or recovery of materials could reduce the surface roughness by reducing the depth of tool marks.

As presented in Fig. 8 (a) and (c), the waviness and PV value of the virgin sample vary with positions, and a similar variation is presented on Ti alloy with EPT of 40 V, which means that the occurrence of material swelling or spring-back is not homogeneous in the two sets of alloys. For workpiece after EPT of 30 V and 60 V, the waviness is relatively even and the fluctuation is not obvious, as shown in Fig. 8 (b) and (d). The average distances of d_1 and d_2 of tool marks are respectively about 4.102 μm and 4.039 μm that are higher than the setting value of 4 μm. Hence, material side swelling occurs in both samples, but the former one is rather remarkable. This is because the soft workpiece could result in a high plastic side flow [33]. In addition, the coupling function of material deep swelling and recovery of the former sample is significant, giving rise to an extremely high PV value (about 150 nm), as shown in Fig. 8 (b). In comparison, the PV value of workpiece after treatment of 60 V is about

31 nm, approximately one-third of alloys with treatment of 30 V, as shown in Fig. 8 (d). Notably, a portion of valley outlines do not fully keep an arc shape and some valleys even show flat features. The formation of irregular shapes is not considered to be caused by the diamond tool wear which might also introduce a flat valley profile, because there are still some valleys remaining as an arc shape. The low PV values and irregular valley outlines demonstrate that deep swelling is non-significant or the spring-back is obvious for the workpiece with EPT of 60 V.

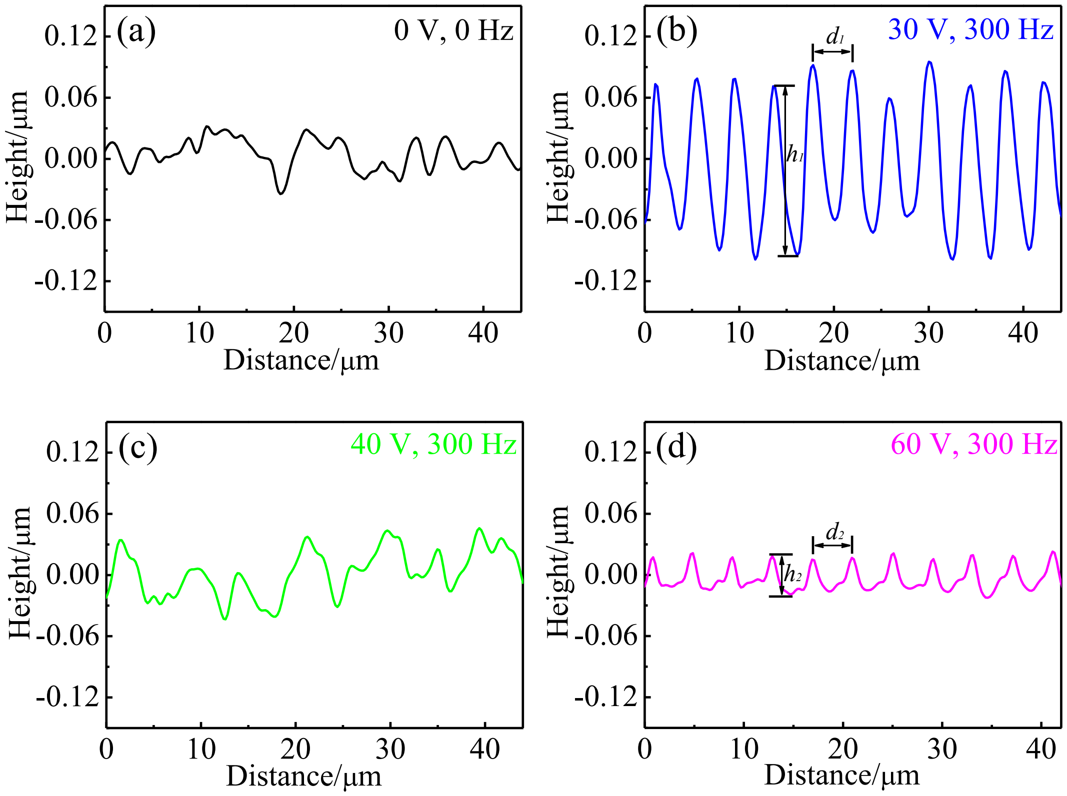

Fig. 8 Cross-section surface profiles of different Ti6Al4V alloys after ultraprecision diamond turning

In order to investigate the effect of material spring-back on the surface turning profiles, straight-line cutting was conducted on the samples with different microstructures. As the cutting grooves show a similar morphology, the alloy after

EPT of 30 V was chosen as an example to analyze the material recovery, as shown in Fig. 9. The material swelling behaviour could be always observed in the turning process, but it was not detected during straight-line cutting without feed rate. Both the groove line curve and AFM morphologies shown in Fig. 9 (b) - (d) verify that the material side flow not occurs during grooves forming. Hence, material recovery could be directly reflected from the groove profiles.

In Fig. 9 (b), the ratio $\vartheta = \frac{\Delta d}{d_c} \times 100\%$ is used to estimate the degree of material spring-back, where Δd is the difference between the ideal surface and real cutting surface and d_c is the cutting depth. The values of the ratio are calculated to be about 5.927 %, 5.946 %, 5.523 %, and 5.706 % for virgin alloy and alloys with EPT of 30 V, 40 V and 60 V respectively. The material recoveries of these alloys could also be reflected from their elastic moduli, as shown in Fig. 9 (e). The small elastic modulus of the alloy with EPT of 30 V means a relative large material recovery, which is in agreement with the material recovery during groove cutting. Consequently, the large PV value of the workpiece after EPT of 30 V indicates that the material deep swelling is more significant in comparison to other samples.

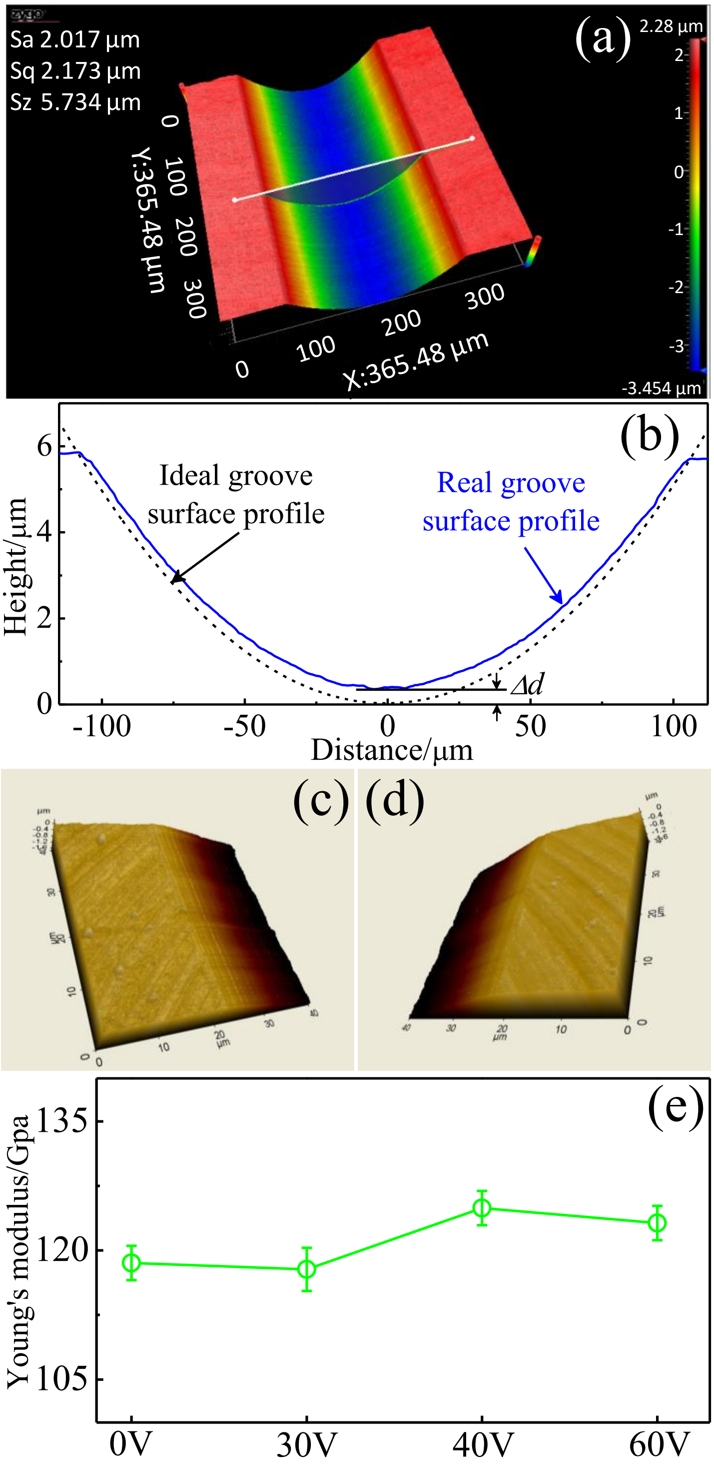

Fig. 9 (A) Cutting groove morphology, (b) surface profiles, (c) and (d) two edges of the alloy after EPT of 30 V; (e) Young's moduli of the alloys with various microstructures.

3.3 Cutting force variation of Ti6Al4V alloys

Fig. 10 shows the variation of main cutting forces and thrust forces of Ti6Al4V alloy with various microstructures. It is clearly seen that cutting and thrust forces show a simultaneous downward trend with the increasing of electropulsing voltage. Especially for EPT of 60 V and 300 Hz, the main cutting force reduces from about 0.65 N to 0.39 N, achieving a force reduction of about 40 %. The dropping amount of thrust forces for EPT of 40V and 60 V is nearly equal to each other, which means that the emergence of lamellar α platelets and decrement of β phase could contribute to the force reduction. Even when the volume fraction of the β phase increases after EPT of 30 V, the cutting forces also drop due to the coarsening of grains. According to the traditional Hall-Petch relationship, the yield stress for plastic deformation would be reduced with the increasing of the average grain size.

Furthermore, the magnitude of force vibration of the alloy after EPT of 30 V is more significant than those with other microstructures, which corresponds to the high PV value shown in Fig. 8 (b). This indicates that the high material side and deep swelling could increase the cutting force fluctuation. For the alloy after EPT of 60 V, periodical sharp tails (black arrows) of cutting and thrust forces are discovered in each of turning cycle, which is supposedly caused by the influence of martensitic orientations of the Ti6Al4V alloy [25].

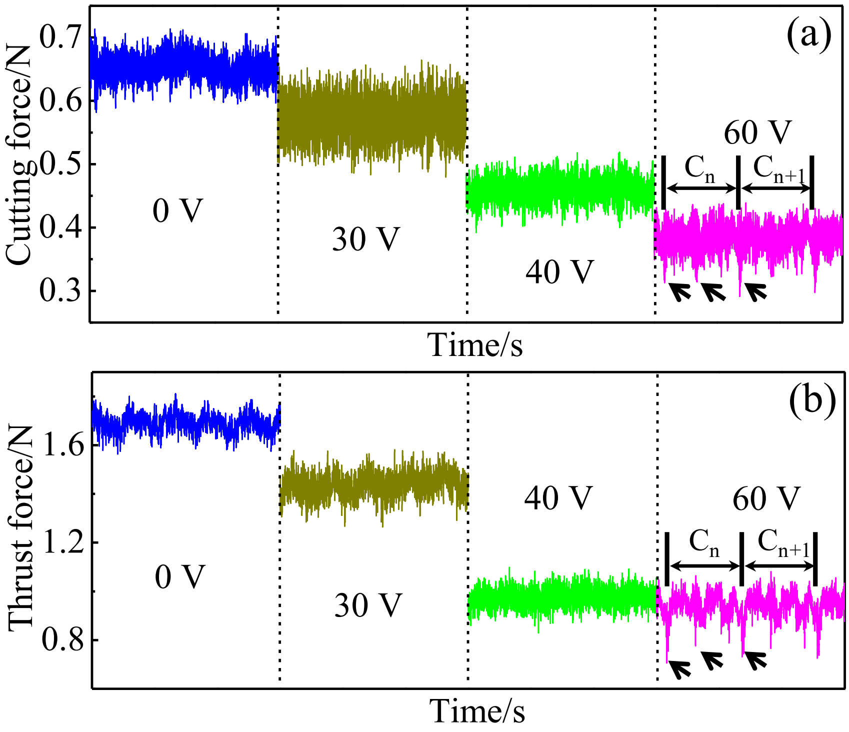

Fig. 10 (A) cutting forces and (b) thrust forces variation in diamond turning of Ti6Al4V alloy with various voltages

4. Discussion

4.1 EPT effects on microstructure evolution of Ti6Al4V alloys

4.1.1 Thermal effects

In comparison to traditional furnace heat treatment, numerous investigations concluded that the EPT could introduce thermal and athermal effects to alter material microstructures when high density of electropulsing passes through metals or alloys [10, 12, 13, 34]. The coupling thermal and athermal effects have potential function to activate the motion of atoms, dislocations and defects, which contributes to the evolution of microstructure of the metals [35].

For the thermal effect, free electrons could be migrated when a voltage (potential difference) is conducted on conductive metals and alloys, and some electrons can collide with atoms located at crystal lattices, which leads to kinetic energy loss of the collided electrons. The lost energy will be scattered in the form of heat. When the instantaneous electrical pulse is sufficiently high, the scattered energy will accumulate rapidly, leading to a very high temperature. The temperature rise can be theoretically expressed as [9]:

$$T_t - T_0 = \frac{\sum \Delta Q}{C_p m} = \frac{\sum \Delta Q}{C_p A_s l D} \tag{1}$$

where T_t is the Kelvin temperature at time *t*, T_0 is room temperature (298.15 K), C_P is the specific heat, A_s, l and D are the cross-sectional area, length (40 mm) and density of the treated alloys, respectively. The net energy $\sum \Delta Q$ retained in the alloy during EPT can be obtained by:

$$\sum \Delta Q = Q_j - Q_t - Q_r - \mathrm{Q_c} \tag{2}$$

where Q_j is the energy obtained from joule thermal effect when electropulsing passes through samples, Q_t and Q_r are energy loss induced by heat transfer and thermal radiation, respectively. $\mathrm{Q_c}$ is the energy transforming from heated workpiece to the two copper electrodes. The obtained energy Q_j is given by [36]:

$$Q_j = \int_0^t (J_e(T) A_s)^2 \frac{\rho(T) l}{A_s} dt = J_e(T)^2 A_s \rho(T) l t_e f t \tag{3}$$

where $J_e(T)$ and $\rho(T)$ are respectively effective current density and electrical resistivity at temperature *T*, t_e is the electropulsing duration of each pulse, and f denotes the electropulsing frequency. The energy loss Q_t due to the heat transfer between samples and air is calculated by [37]:

$$Q_t = \alpha S(T_t - T_0)t$$

(4)

where S is total surface area of samples, and α denotes the heat transfer coefficient , which is estimated as follows [38]:

$$\alpha = \frac{N_u k}{2r} \tag{5}$$

where r is the radius of samples, k is the thermal conductivity, and N_u is the Nusselt number that could be evaluated by the following equation in a cylinder [39]:

$$N_u = CRa_D^n \tag{6}$$

where C and n are variables that are determined by the Rayleigh number (Ra_D), and the expression for Ra_D is [40]:

$$Ra_D = \frac{4g\beta'\Delta T r^2}{v^2} Pr$$

(7)

where g is the acceleration of gravity, ΔT is temperature difference between workpiece and air, v is the kinematic viscosity, Pr is the Prandtl number, and β' is the coefficient of thermal expansion. The energy radiation to air Q_r can be estimated from the well-known Stefan-Boltzmann Law [41]:

$$Q_r = \sigma T_t^4 St$$

(8)

where σ is called the Stefan-Boltzmann constant (σ=5.67×10^{-8} W·m^{-2}·K^{-4}). The transferred energy Q_c from workpiece to the two copper electrodes could be given by [40]:

$$Q_t = 2\alpha_c A_s(T_t - T_0)t$$

(9)

where α_c is the interface heat transfer coefficient between workpiece and copper electrodes, and the average value is about 2×10^3 W/ m^2 K for copper in solid contact condition [40]. The effective current density, electrical resistivity and density of Ti6Al4V alloys are assumed to be independent of temperature; therefore, the final equation to estimate the temperature evolution during the EPT process is formulated as follows:

$$T_t - T_0 = \frac{{J_e}^2 A_s \rho l t_e f t - \alpha S(T_t - T_0)t - \sigma T_t^4 S t}{C_p A_s l D} = \frac{{J_e}^2 \rho t_e f t}{C_p D} - \frac{2\alpha(T_t - T_0)t + 2\sigma T_t^4 t}{C_p r D} - \frac{2\alpha_c(T_t - T_0)t}{C_p l D} \quad (10)$$

For any conductive metals or alloys under electropulsing treatment, the temperature at a certain time can be evaluated from equation (10). Table 2 lists the relative parameters of Ti6Al4V alloy. The parameters tabulated in Table 3 are based on different temperatures induced by various EPT voltages, which are used to calculate the heat transfer coefficient between workpiece and air.

Table 2 Parameters of Ti6Al4V alloy from relevant references

Parameters	Values	Ref.
ρ(Ω·m)	1.78×10^{-6}	[42]
C_p(J/kg °C)	5.46×10^{2}	[43]
D(kg/m^3)	4.42×10^{3}	[43]

Table 3 Parameters for calculation of the heat transfer coefficient

Parameters	0V	30V	40V	60V	Ref.
$k(W/m\,K)$	2.63×10^{-2}	5.73×10^{-2}	7.10×10^{-2}	0.10	[44]

$\beta'(1/K)$	3.41×10^{-3}	1.29×10^{-3}	9.72×10^{-4}	7.9×10^{-4}	[40]
$v(\mathrm{m^2/s})$	1.59×10^{-5}	8.49×10^{-5}	1.42×10^{-4}	2.40×10^{-4}	[44]
Pr	0.707	0.709	0.728	0.685	[44]

Fig. 11 compares the temperature evolution of theoretically calculated data from equation (10) and measured data from the digital thermocouple. At the beginning, the calculated temperature is slightly higher than that of measured values, but the gap clearly narrows after EPT for 15 s, which means that the calculated data of alloys under various EPT conditions is in accordance with the corresponding measurement data at relatively high temperatures. Furthermore, the temperature rising rates are diverse for different EPT parameters. Increase in voltages tends to elevate the temperature rising rate and the terminal temperature. For the sample with EPT of 60 V and 300 Hz, the rising rate is about 110-133.4 °C/s at the temperature-rise period. After that, the rising rate gradually falls over time, and finally a dynamic thermal equilibrium is achieved at high temperature in which condition the generated energy from electropulsing is equal to the energy loss induced by heat transfer and thermal radiation.

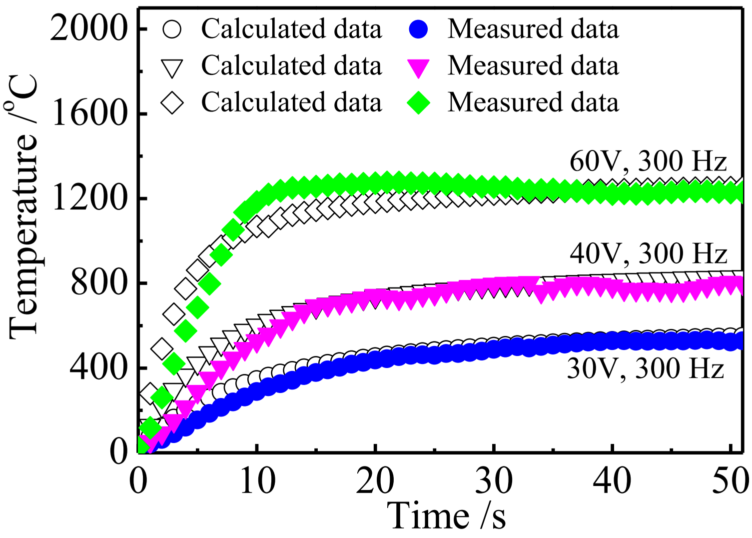

Fig. 11 Simulated and measured temperature evolution

4.1.2 Athermal effects

The athermal effect is another important factor to facilitate the microstructure evolution and phase transformation of metals or alloys, and it is functioned by a so called "electron wind" generated from the electropulsing. The mechanism of microstructure evolution is closely associated with the generation and migration of dislocation in the lattice and grain or sub-grain boundaries. In conventional heat treatment of Ti6Al4V alloys, ageing for several hours or even days is usually needed to guarantee microstructure changes and phase transformation. However, microstructures and phases of titanium alloys could be altered within a few minutes with the assistance of high current density. The generated electron wind has the potential to accelerate the motion of dislocations, and the motivated dislocations could even reach an ultrasonic speed, so the transferred energy from electropulsing to atoms is extremely effective in comparison with the traditional heat treatment. The atomic diffusion flux j_a is due to the athermal effect and can be expressed as follows [10]:

$$j_a = \frac{D_i}{kT}(K_{ew}\Omega j_m + N_i Re Z_i^* j_m)$$

(11)

where D_i and N_i are the diffusion coefficient and density of atom i, respectively; k is the Bolzmann constant, T is the absolute temperature, K_{ew} stands for the electron wind force coefficient, Ω is the atom volume, R is the specific resistivity, eZ_i^* denotes the effective charges of inter-crystalline atoms and j_m is the electropulsing peak current density. The first term on the right hand side (RHS) of equation (5) denotes the dislocation and vacancy fluxes resulted from the effect of electron wind force. The second term on the RHS represents vacancies from atom self-diffusion during EPT process. With the increasing of electropulsing voltages from 30 V to 60 V, the corresponding peak current density j_m passing through Ti6Al4V alloys will also be increased. Hence, both the dislocation and vacancy fluxes and their motions are improved by raising EPT voltages, giving rise to an enhancement of athermal effects. In addition, the thermodynamic barrier for phase transformation from α to β of titanium alloys may be reduced by the athermal effect [12, 45].

The athermal effect is activated simultaneously with the thermal effect, and the coupling function of the two effects is likely to be the most acceptable mechanism for explaining the microstructure evolution after EPT, because both of them have the ability to promote the motion of atoms, dislocations and defects.

4.2 Qualitative analysis of cutting and thrust forces

The flow stress of Ti6Al4V alloys is closely correlated with the microstructure in ultraprecision diamond turning, which can be directly reflected from the microhardness and variations in the cutting force. For the workpiece with EPT of 30 V, the corresponding microhardness and cutting and thrust force both have a minor decrease due to the grain growth, and this is in agreement with the Hall-Petch relationship. However, with further increasing of EPT voltages, the variation of microhardness and cutting and thrust forces shows an opposite changing trend, which conflicts with the common knowledge that the forces should be elevated with the increase of hardness. Generally, factors that affect the forces can be briefly summarized as machine tools (tool category, tool geometry and tool wear), cutting conditions, surroundings and material properties. The machine tool, cutting parameters and environment conditions are all same during turning of the Ti6Al4V alloys in this study, so variations in the force should be mainly induced by the material factors, mainly including material microstructures, material swelling and adhesion of tool-chip interface. A model based on Fig. 12 is built up to estimate the variation of the main cutting force F_c and thrust force F_t, as follows:

$$F_c = F_m cos\varphi + F_{f2}$$

(12-1)

$$F_t = F_m sin\varphi + F_s + F_{f1}$$

(12-2)

where F_{f1} is a friction force between the tool and cutting chips, F_{f2} is a tool-workpiece frictional force, which is assumed to be same at the same depth of cut. F_s is a force caused by the material spring-back, φ is the shear angle that could be estimated by the chip thickness ratio [46]:

$$\frac{t_0}{t_c} = \frac{sin\varphi}{cos\,(\varphi - \alpha)} \qquad (13)$$

where t_0 and t_c are cutting depth and measured chip thickness after turning, respectively. The tool rake angle α is equal to zero in this study. The force F_m in equation (12) refers to the stress required to overcome the material inner stresses in the shear band, including critical resolve shear stress (CRSS), barrier stresses resulting from grain or phase boundaries and dislocations, and dislocation drag stress under high strain rate. Hence, the stress τ_m in the deformation zone can be expressed by [47]:

$$\tau_m = \tau_c + \tau_g + \tau_d + \tau_d' = \tau_c + \frac{\alpha_g \mu \sqrt{b}}{\sqrt{d}} + \alpha_\rho \mu b \sqrt{\rho_d} + \alpha_d \dot{\varepsilon} \tag{14}$$

where τ_c is the CRSS for plastic deformation, τ_g, τ_d and τ_d' are stresses induced by the grain or phase boundaries and dislocations, respectively; α_g, α_ρ and α_d are constants, μ is the shear modulus depending on temperature, b is the Burgers vector, d is the average grain size, ρ_d is the dislocation density and $\dot{\varepsilon}$ is the strain rate.

The volume fraction of β phase with bcc crystal structure increases after EPT of 30 V. As the slip system of bcc structure is higher than that of hcp structural α phase, increase in β phase content results in a relatively small CRSS. Furthermore, the stress to overcome material deformation is also reduced because grains are coarsened after EPT. Hence, the required stress τ_m to overcome plastic flow should be decreased after EPT of 30 V. In addition, the chip thickness of the alloy after EPT of 30 V is slightly smaller than that without EPT, as shown in Fig. 13 (a) and (b). As the depth of cut is the same, the relative small chip thickness indicates that the shear angle of the EPT treated alloy is slightly larger than that of the virgin alloy according to equation (13). Consequently, the required applied force should decrease after EPT of 30 V.

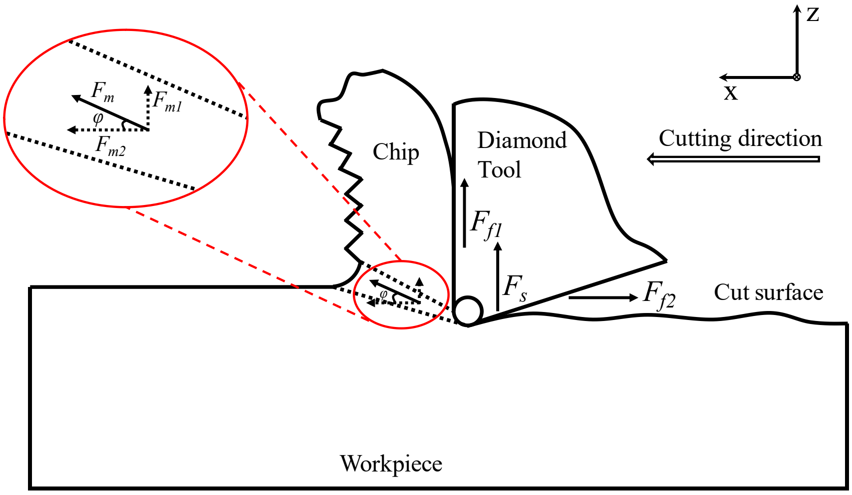

Fig. 12 Schematic diagram of the thrust force in ultraprecision machining

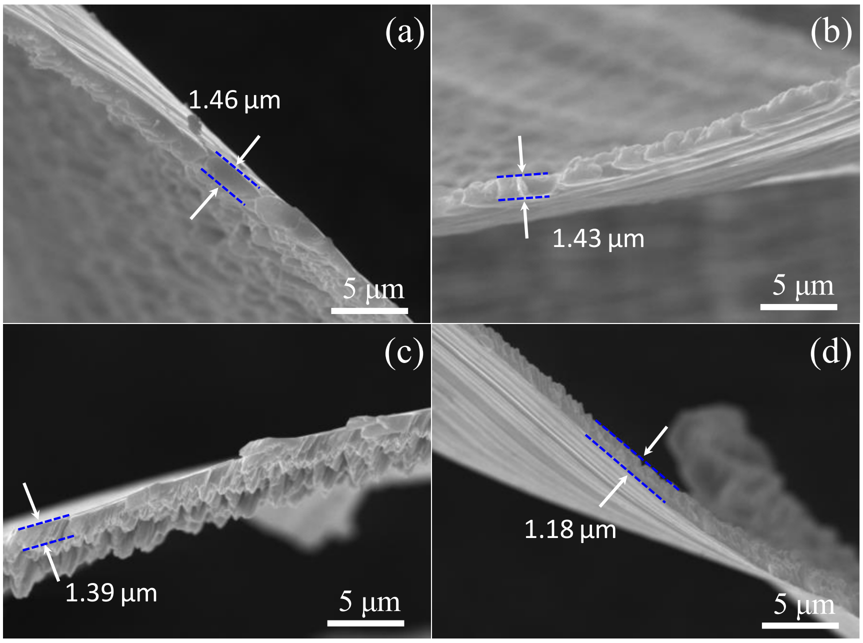

Fig. 13 Cutting chip morphologies of alloys after EPT of (a) 0 V, (b) 30 V, (c) 40 V and (d) 60 V

For samples with EPT of 40 V and 60 V, as the microstructures are completely different from these of virgin and EPT 30 V treated ones, the deformation mechanism should not be same. After EPT of 60 V, α colonies consisting of martensitic α prevail in the Ti6Al4V alloy and rare β phase can be observed from both SEM morphologies and XRD patterns. The presence of martensitic α lamellas could lead to poor ductility

[7, 48]. Materials with inferior ductility are prone to generating a smaller built-up edge (BUE) and a minor material side flow during cutting [33], so the workpiece with lamellar structure possesses slightly wide tool marks after turning.

The yield stress required to plastic deformation of the alloy with lamellar microstructure is larger than that of the alloy with bimodal structures [7, 48]; hence, the required force F_m to overcome plastic flow is higher for ETP of 60 V. However, the cutting force after EPT of 60 V is lower than the force after EPT of 40V, which indicates that the shear angle of the former sample with lamellar martensites should be higher than the sample with bimodal structure during diamond turning process. The thinner chip thickness observed in Fig. 13 (d) accurately verifies that the alloy with lamellar structure possesses a large shear angle in turning.

As for the variation of the thrust force after EPT of 40 V and 60V, the increasing of shear angle after EPT of 60V contributes to the increase in component stress in the thrust force direction. In addition, the force F_s in equation (6-2) of the workpiece after EPT of 60 V is also higher than that of EPT of 40V due to the slightly large material spring-back. However, the first two terms of RHS of equation (6-2) could not contribute to the thrust force rising, but instead the force slightly declines from 0.97 N to 0.94 N. Therefore, the last term representing the tool-chip friction force in equation (12-2) is supposed to be much smaller for workpiece with lamellar martensites, and the reduction amount should be higher than the increased forces caused by deformation and material spring-back.

5. Conclusion

Ti6Al4V alloys with equiaxial, bimodal and martensitic microstructures were obtained by electropulsing treatment at voltages of 30 V, 40V and 60 V, respectively. Then, ultraprecision machining was executed to investigate the machinability of these alloys. The results of this study can be summarized as follows:

(1) The microstructure evolution is primarily attributed to the combined function of thermal and athermal effects. The model based on energy gain, heat transfer and thermal radiation could precisely estimate the temperature evolution induced by the thermal effect of EPT. The dislocation and vacancy motion could be accelerated by the athermal effect of EPT, and the effect enhances with the increasing of EPT voltages.

(2) The machinability of Ti6Al4V varies with microstructures. For alloys with coarsened equiaxed grains after EPT of 30 V, the area surface roughness and PV value reach as high as about 52 nm and 150 nm, respectively; while the alloy with fully lamellar martensites possesses the lowest surface roughness (9 nm) and PV value (31 nm) after diamond turning. The various turning surface profiles are mainly due to the different swelling and recovery of the Ti6Al4V alloys.

(3) The qualitative cutting and thrust force analyses of the Ti6Al4V alloy after EPT with different voltages demonstrate that the force reduction after EPT of 30 V is due to the grain growth. For workpiece with lamellar structure achieved by EPT of 60 V, the friction force between tool and chips is much smaller in comparison to the alloys with bimodal microstructure.

Acknowledgement

The work described in this paper was partially supported by a grant from the Research Committee (Project No. G-YBLE) and Partner State Key Laboratory of Ultra-precision Machining Technology (Project No. 1-BBX7) of the Hong Kong Polytechnic University.

References

[1] M.K. Kulekci. Magnesium and its alloys applications in automotive industry. Int J Adv Manuf Tech 2008;39:851-865.

[2] D.R. Floyd, J.N. Lowe. Beryllium science and technology. Springer; 2014.

[3] C. Veiga, J. Davim, A. Loureiro. Properties and applications of titanium alloys: a brief review. Rev Adv Mater Sci 2012;32:133-148.

[4] T. Ahmed, H. Rack. Phase transformations during cooling in α+ β titanium alloys. Mat Sci Eng A 1998;243:206-211.

[5] S. Semiatin, T. Bieler. The effect of alpha platelet thickness on plastic flow during hot working of Ti–6Al–4V with a transformed microstructure. Acta Mater 2001;49:3565-3573.

[6] M. Jovanović, S. Tadić, S. Zec, Z. Mišković, I. Bobić. The effect of annealing temperatures and cooling rates on microstructure and mechanical properties of investment cast Ti–6Al–4V alloy. Mater Design 2006;27:192-199.

[7] H. Matsumoto, H. Yoneda, K. Sato, S. Kurosu, E. Maire, D. Fabregue, T.J. Konno, A. Chiba. Room-temperature ductility of Ti–6Al–4V alloy with α′ martensite microstructure. Mat Sci Eng A 2011;528:1512-1520.

[8] O. Troitskii. Effect of the electron state of a metal on its mechanical properties and

the phenomenon of electroplasticity. Strength Mater 1977;9:35-45.

[9] W. Zhang, M. Sui, Y. Zhou, D. Li. Evolution of microstructures in materials induced by electropulsing. Micron 2003;34:189-198.

[10] S. To, Y. Zhu, W. Lee, X. Liu, Y. Jiang, G. Tang. Effects of current density on electropulsing-induced phase transformations in a Zn–Al based alloy. Appl Phys A 2009;96:939-944.

[11] S.S. To, H. Wang, W.B. Lee. Materials Characterisation and Mechanism of Micro-Cutting in Ultra-Precision Diamond Turning. Springer; 2018.

[12] Y. Jiang, G. Tang, C. Shek, Y. Zhu, Z. Xu. On the thermodynamics and kinetics of electropulsing induced dissolution of β-Mg17Al12 phase in an aged Mg–9Al–1Zn alloy. Acta Mater 2009;57:4797-4808.

[13] H. Wang, G. Song, G. Tang. Evolution of surface mechanical properties and microstructure of Ti6Al4V alloy induced by electropulsing-assisted ultrasonic surface rolling process. J Alloy Compd 2016;681:146-156.

[14] H.B. Wu, S. To. Effects of electropulsing treatment on material properties and ultra-precision machining of titanium alloy. Int J Adv Manuf Tech 2016;82:2029-2036.

[15] D. Ao, X. Chu, Y. Yang, S. Lin, J. Gao. Effect of electropulsing treatment on microstructure and mechanical behavior of Ti-6Al-4V alloy sheet under argon gas protection. Vacuum 2018;148:230-238.

[16] S. Sartori, A. Ghiotti, S. Bruschi. Temperature effects on the Ti6Al4V machinability using cooled gaseous nitrogen in semi-finishing turning. J Manuf

Process 2017;30:187-194.

[17] R. Khettabi, L. Fatmi, J. Masounave, V. Songmene. On the micro and nanoparticle emission during machining of titanium and aluminum alloys. CIRP J Manuf Sci Tec 2013;6:175-180.

[18] K. Venugopal, S. Paul, A. Chattopadhyay. Growth of tool wear in turning of Ti-6Al-4V alloy under cryogenic cooling. Wear 2007;262:1071-1078.

[19] S. Sun, M. Brandt, S. Palanisamy, M.S. Dargusch. Effect of cryogenic compressed air on the evolution of cutting force and tool wear during machining of Ti–6Al–4V alloy. J Mater Process Tech 2015;221:243-254.

[20] A. Shokrani, V. Dhokia, S.T. Newman. Investigation of the effects of cryogenic machining on surface integrity in CNC end milling of Ti–6Al–4V titanium alloy. J Manuf Process 2016;21:172-179.

[21] M. Nouari, H. Makich. Experimental investigation on the effect of the material microstructure on tool wear when machining hard titanium alloys: Ti–6Al–4V and Ti-555. Int J Refract Met H 2013;41:259-269.

[22] M. Armendia, P. Osborne, A. Garay, J. Belloso, S. Turner, P.-J. Arrazola. Influence of heat treatment on the machinability of titanium alloys. Mater Manuf Process 2012;27:457-461.

[23] A. Attanasio, M. Gelfi, A. Pola, E. Ceretti, C. Giardini. Influence of material microstructures in micromilling of Ti6Al4V alloy. Materials 2013;6:4268-4283.

[24] M. Ahmadi, Y. Karpat, O. Acar, Y.E. Kalay. Microstructure effects on process outputs in micro scale milling of heat treated Ti6Al4V titanium alloys. J Mater

Process Tech 2018;252:333-347.

[25] Z. Zhao, S. To. An investigation of resolved shear stress on activation of slip systems during ultraprecision rotary cutting of local anisotropic Ti-6Al-4V alloy: Models and experiments. Int J Mach Tool Manu 2018.

[26] E. Sallica-Leva, R. Caram, A. Jardini, J. Fogagnolo. Ductility improvement due to martensite α′ decomposition in porous Ti–6Al–4V parts produced by selective laser melting for orthopedic implants. J Mech Behav Biomed 2016;54:149-158.

[27] W. Sha, Z. Guo. Phase evolution of Ti–6Al–4V during continuous heating. J Alloy Compd 1999;290:L3-L7.

[28] S. Roy, S. Suwas, S. Tamirisakandala, D.B. Miracle, R. Srinivasan. Development of solidification microstructure in boron-modified alloy Ti–6Al–4V–0.1 B. Acta Mater 2011;59:5494-5510.

[29] M. Bermingham, J. Thomson-Larkins, D. St John, M. Dargusch. Sensitivity of Ti-6Al-4V components to oxidation during out of chamber Wire+ Arc Additive Manufacturing. J Mater Process Tech 2018;258:29-37.

[30] G. Lütjering, J.C. Williams. Beta Alloys. Springer; 2007.

[31] F. Gil, M. Ginebra, J. Manero, J. Planell. Formation of α-Widmanstätten structure: effects of grain size and cooling rate on the Widmanstätten morphologies and on the mechanical properties in Ti6Al4V alloy. J Alloy Compd 2001;329:142-152.

[32] S. To, C. Cheung, W. Lee. Influence of material swelling on surface roughness in diamond turning of single crystals. Mater Sci Tech Ser 2001;17:102-108.

[33] D.J. Whitehouse. Handbook of surface and nanometrology. CRC press; 2010.

[34] Z. Xu, G. Tang, S. Tian, J. He. Research on the engineering application of multiple pulses treatment for recrystallization of fine copper wire. Mat Sci Eng A 2006;424:300-306.

[35] Y. Zhu, S. To, W. Lee, X. Liu, Y. Jiang, G. Tang. Effects of dynamic electropulsing on microstructure and elongation of a Zn–Al alloy. Mat Sci Eng A 2009;501:125-132.

[36] R. Zhu, J. Liu, G. Tang, S. Shi, M. Fu. Properties, microstructure and texture evolution of cold rolled Cu strips under electropulsing treatment. J Alloy Compd 2012;544:203-208.

[37] T.L. Bergman, F.P. Incropera, A.S. Lavine, D.P. Dewitt. Introduction to heat transfer. John Wiley & Sons; 2011.

[38] S. Kakaç, A. Pramuanjaroenkij. Review of convective heat transfer enhancement with nanofluids. Int J Heat Mass Tran 2009;52:3187-3196.

[39] V.T. Morgan. The overall convective heat transfer from smooth circular cylinders. In: Advances in heat transfer, Elsevier; 1975, p. 199-264.

[40] F. Kreith, R.M. Manglik, M.S. Bohn. Principles of heat transfer. Cengage learning; 2012.

[41] S.B. Giddings. Hawking radiation, the Stefan–Boltzmann law, and unitarization. Phys Lett B 2016;754:39-42.

[42] P. Fonda, Z. Wang, K. Yamazaki, Y. Akutsu. A fundamental study on Ti–6Al–4V's thermal and electrical properties and their relation to EDM productivity. J Mater Process Tech 2008;202:583-589.

[43] J. Yang, S. Sun, M. Brandt, W. Yan. Experimental investigation and 3D finite element prediction of the heat affected zone during laser assisted machining of Ti6Al4V alloy. J Mater Process Tech 2010;210:2215-2222.

[44] T.L. Bergman, F.P. Incropera, D.P. DeWitt, A.S. Lavine. Fundamentals of heat and mass transfer. John Wiley & Sons; 2011.

[45] X. Ye, G. Tang, G. Song, J. Kuang. Effect of electropulsing treatment on the microstructure, texture, and mechanical properties of cold-rolled Ti–6Al–4V alloy. J Mater Res 2014;29:1500-1512.

[46] M.E. Merchant. Mechanics of the metal cutting process. I. Orthogonal cutting and a type 2 chip. J Appl Phys 1945;16:267-275.

[47] S.N. Melkote, R. Liu, P. Fernandez-Zelaia, T. Marusich. A physically based constitutive model for simulation of segmented chip formation in orthogonal cutting of commercially pure titanium. CIRP Ann 2015;64:65-68.

[48] R. Nalla, R. Ritchie, B. Boyce, J. Campbell, J. Peters. Influence of microstructure on high-cycle fatigue of Ti-6Al-4V: bimodal vs. lamellar structures. Metall Mater Trans A 2002;33:899-918.